Low-frequency pulse profile variation in PSR B2217+47: evidence for echoes from the interstellar medium

D. Michilli,[1,2]⋆ J. W. T. Hessels,[1,2] J. Y. Donner,[3] J.-M. Grießmeier,[4,5] M. Serylak,[6,7]
B. Shaw,[8] B. W. Stappers,[8] J. P. W. Verbiest,[3,9] A. T. Deller,[10] L. N. Driessen,[1,8]
D. R. Stinebring,[11] L. Bondonneau,[4] M. Geyer,[12] M. Hoeft,[13] A. Karastergiou,[12,6,14]
M. Kramer,[9,8] S. Osłowski,[10] M. Pilia,[15,2] S. Sanidas[1] and P. Weltevrede[8]

[1]*Anton Pannekoek Institute for Astronomy, University of Amsterdam, Science Park 904, NL-1098 XH Amsterdam, the Netherlands*
[2]*ASTRON, the Netherlands Institute for Radio Astronomy, Postbus 2, NL-7990 AA, Dwingeloo, the Netherlands*
[3]*Fakultät für Physik, Universität Bielefeld, Postfach 100131, D-33501 Bielefeld, Germany*
[4]*LPC2E – Université d'Orléans / CNRS, F-45071 Orléans CEDEX 2, France*
[5]*Station de Radioastronomie de Nançay, Observatoire de Paris, PSL Research University, CNRS, Univ. Orléans, OSUC, F-18330 Nançay, France*
[6]*Department of Physics and Astronomy, University of the Western Cape, Private Bag X17, Bellville 7535, South Africa*
[7]*SKA South Africa, 3rd Floor, The Park, Park Road, Pinelands, Cape Town 7405, South Africa*
[8]*Jodrell Bank Centre for Astrophysics, School of Physics and Astronomy, The University of Manchester, Manchester M13 9PL, UK*
[9]*Max-Planck-Institut für Radioastronomie, Auf dem Hügel 69, D-53121 Bonn, Germany*
[10]*Centre for Astrophysics and Supercomputing, Swinburne University of Technology, PO Box 218, Hawthorn, VIC 3122, Australia*
[11]*Department of Physics and Astronomy, Oberlin College, 110 North Professor St., Oberlin, OH 44074, USA*
[12]*Oxford Astrophysics, Denys Wilkinson Building, Keble Road, Oxford OX1 3RH, UK*
[13]*Thüringer Landessternwarte Tautenburg, Sternwarte 7, D-07778 Tautenburg, Germany*
[14]*Department of Physics and Electronics, Rhodes University, PO Box 94, Grahamstown 6140, South Africa*
[15]*INAF – Osservatorio Astronomico di Cagliari, via della Scienza 5, I-09047 Selargius (Cagliari), Italy*

ABSTRACT

We have observed a complex and continuous change in the integrated pulse profile of PSR B2217+47, manifested as additional components trailing the main peak. These transient components are detected over 6 yr at 150 MHz using the LOw Frequency ARray (LOFAR), but they are not seen in contemporaneous Lovell observations at 1.5 GHz. We argue that propagation effects in the ionized interstellar medium (IISM) are the most likely cause. The putative structures in the IISM causing the profile variation are roughly half-way between the pulsar and the Earth and have transverse radii $R \sim 30$ au. We consider different models for the structures. Under the assumption of spherical symmetry, their implied average electron density is $\overline{n}_e \sim 100$ cm^{-3}. Since PSR B2217+47 is more than an order of magnitude brighter than the average pulsar population visible to LOFAR, similar profile variations would not have been identified in most pulsars, suggesting that subtle profile variations in low-frequency profiles might be more common than we have observed to date. Systematic studies of these variations at low frequencies can provide a new tool to investigate the proprieties of the IISM and the limits to the precision of pulsar timing.

Key words: pulsars: individual: PSR B2217+47 – ISM: general – radio continuum: ISM.

1 INTRODUCTION

When averaged over hundreds of rotational periods, pulsars typically show stable integrated pulse profiles over time-scales of years to decades (Helfand, Manchester & Taylor 1975; Liu et al. 2012). The stability of the integrated pulsar emission is key to using pulsars as 'astrophysical clocks' in timing experiments (Manchester 2017). However, subtle, long-time-scale variations sometimes exist, and can be either intrinsic to the pulsar magnetosphere (Hobbs, Lyne & Kramer 2010) or due to varying propagation effects as the signal travels through the ionized interstellar medium (IISM, Keith et al. 2013). Studying pulse profile changes in radio pulsars is thus motivated by both understanding the underlying physical mechanisms responsible for the observed changes and by improving the precision of pulsar timing experiments.

⋆ E-mail: danielemichilli@gmail.com

Only a small fraction of isolated pulsars have been observed to manifest a continuous pulse profile evolution. Stairs, Lyne & Shemar (2000) attributed the quasi-periodic profile variation of PSR B1828−11 to free precession of the neutron star. Lyne et al. (2010) questioned this interpretation when they found quasi-periodic profile changes in six pulsars (including PSR B1828−11), which are correlated with the spin-down rate and thus likely originate from processes intrinsic to the source. External factors have also been invoked to explain observed profile variations: For example, Karastergiou et al. (2011) reported a pulse profile variation for PSR J0738−4042 attributed to magnetospheric changes, which Brook et al. (2014) connected to an interaction with an asteroid. A systematic search by Brook et al. (2016) found seven examples of profile change in a sample of 168 pulsars, a subset of which were correlated with $\dot{\nu}$ variations. Osłowski et al. (in preparation) observed a profile variation of PSR B1508+55 presenting characteristics similar to the one reported here for PSR B2217+47. They attribute the variation to IISM propagation effects.

Pulsar signals propagate through the IISM before reaching the Earth, and this imparts several features on the observed signal (e.g. Rickett 1990). Among these, dispersion is the frequency-dependent light traveltime due to free electrons along the line of sight (LoS), where the integrated column density is quantified by the dispersion measure (DM, Lorimer & Kramer 2004). A second propagation effect is scintillation, and it is due to inhomogeneities in the IISM electron density (Rickett 1990). A peculiar manifestation of propagation effects is an extreme scattering event (ESE, Fiedler et al. 1987). During an ESE, a dense plasma structure of finite size crosses the LoS to a point source. This can lead to different detectable variations in the signal (e.g. in the source flux, Fiedler et al. 1987; Cognard et al. 1993). Thus far, variations in a pulsar's average profile due to dense structures crossing the LoS have only been reported in the form of echoes produced by the Crab nebula surrounding PSR B0531+21 (Backer, Wong & Valanju 2000; Lyne, Pritchard & Graham-Smith 2001). Another manifestation of propagation effects in pulsar observations is scintillation arcs. These are parabolic arcs visible in some pulsars' secondary spectra, i.e. the two-dimensional Fourier transform of the signal as a function of frequency and time (Stinebring et al. 2001). They are thought to be produced by scintillation caused by thin screens along the LoS.

In recent years, a new generation of radio telescopes such as the LOw Frequency ARray (LOFAR, van Haarlem et al. 2013), the Murchison Widefield Array (MWA, Tingay et al. 2013) and the Long Wavelength Array (LWA, Taylor et al. 2012) have renewed interest in pulsar studies at frequencies below 300 MHz, including investigations of pulse profiles. Low-frequency studies potentially allow for more sensitive analyses of profile variability, both if the cause is intrinsic to the pulsar emission or due to propagation effects. In fact, the radius-to-frequency-mapping model (Ruderman & Sutherland 1975; Cordes 1975) states that lower frequency radio waves are emitted at higher altitudes above the neutron star's magnetic poles, which implies a larger cone of emission at lower frequencies and hence amplified angular-dependent variations in pulsar beams. Likewise, low-frequency radio waves are far more sensitive to propagation effects in the IISM.

Here, we present a comprehensive study of profile variations in PSR B2217+47 (J2219+4754), a slow pulsar discovered by Taylor & Huguenin (1969). With a mean flux density of 820 ± 410 mJy at 150 MHz (Bilous et al. 2016), PSR B2217+47 is one of the brightest pulsars in the low-frequency sky. This allows even subtle profile changes to be detected. The pulse profile of PSR B2217+47 is typically single-peaked below 300 MHz (e.g. Kuzmin et al. 1998).

However, we noticed that the single-epoch LOFAR 150 MHz profile reported in Pilia et al. (2016) shows a prominent trailing secondary component.[1] Intriguingly, using the BSA telescope at the Pushchino Observatory at a central frequency of 102.5 MHz, Suleymanova & Shitov (1994) previously reported variations in the pulse profile of PSR B2217+47. They detected a similar secondary component appearing and evolving between 1983 and 1984 and again between 1987 and 1992. This feature was not detected at 325 MHz in 2006–2007 (Mitra & Rankin 2011), nor was it seen by Basu, Mitra & Rankin (2015); the authors report the absence of the transient component in profiles at higher frequency, but they do not give additional information on the observations. Suleymanova & Shitov (1994) attributed the evolving component to pulsar free precession. As an alternative explanation, significant DM changes detected towards PSR B2217+47 suggest a strongly inhomogeneous IISM along the pulsar's LoS (Ahuja et al. 2005). The DM of the source increased by 0.02 pc cm^{-3} over ∼400 d in 2001–2002, decreasing again in the following ∼100 d (Ahuja et al. 2005). This was the only systematic DM variation among a sample of 12 pulsars reported by Ahuja et al. (2005).

We performed a dense, multifrequency campaign, with LOFAR observations beginning in 2011. The observations used in this study are described in Section 2 along with the processing methods employed. In Section 3, we analyse the changes in the pulsar characteristics as a function of time. Different scenarios for the origin of these variations and their implications are discussed in Section 4. An IISM interpretation is favoured by the observations, and we develop the model in Section 5. We conclude the study by summarizing our findings in Section 6.

2 OBSERVATIONS AND DATA PROCESSING

The analysis presented in this paper is based on the observations summarized in Table 1. Times of arrival (TOAs) between 1969 December and 1982 May were obtained by Downs & Reichley (1983) using the NASA Deep Space Network. Jodrell Bank observations span 32 yr, primarily using the 76-m Lovell telescope. Occasional supplementary observations were made using the 38×25-m Mark II telescope. They are included in the Jodrell Bank data archive of pulsar observations (Hobbs et al. 2004). Detailed information on Lovell and Mark II observations and data analysis are provided by Shemar & Lyne (1996), Gould & Lyne (1998), and Hobbs et al. (2004). LOFAR observations span 6 yr. Pulsar observing with LOFAR is extensively described by Stappers et al. (2011). All the observations presented here have been acquired using the high-band antennas (HBAs), which observe at a central frequency of ∼150 MHz. Low-band antenna (LBA) observations, which have a central frequency of ∼50 MHz, were not used because PSR B2217+47 is heavily scattered at these frequencies (Pilia et al. 2016), and this masks the subtle profile variations studied here. The scattering itself might also be variable, but we were unable to investigate this due to the small number of available LBA observations and their limited sensitivity. We used observations acquired with both the LOFAR core and international stations. We used five international LOFAR stations in stand-alone (local recording) mode: DE601 in Effelsberg, DE603 in Tautenburg, DE605 in Jülich, FR606 in Nançay, and UK608 in Chilbolton. The observations were taken using different telescope configurations and different time and frequency resolutions, as summarized in Table 1.

---

[1] www.epta.eu/epndb

Table 1. Summary of the observations used to form our data set. TOAs were calculated for all the observations except where indicated otherwise. Pulse profiles were obtained from all the observations after 2011 March.

Telescope	Centre frequency (MHz)	Bandwidth (MHz)	Typical integration time (min)	Number of observations	Timespan
LOFAR core	122–151	2–92	5	17[a]	2011 Mar–2012 Nov
LOFAR core	149	78	10	40	2013 Dec–2017 Feb
DE601	145	36	15	23	2013 Jun–2013 Jul
DE601	139	48	30	7	2013 May–2013 Aug
DE601	157	61	20	2[a]	2013 Aug–2013 Sep
DE601	154	54	13	2[a]	2013 Dec
DE601	149	78	90	18	2013 Aug–2015 Jun
DE603	149	78	10	10	2014 Feb–2014 May
DE605	149	78	70	9	2014 Dec–2015 Jan
DE605	158	64	100	22	2015 May–2015 Jul
FR606	162	48	30	9	2014 Feb–2014 May
FR606	149	78	120	1[a]	2014 May
UK608	167	48	60	11[a]	2013 Jun–2013 Nov
UK608	161–164	36	60	3[a]	2013 Jul–2015 May
UK608	162	48	60	22	2013 Jun–2015 Oct
Mark II	1400	32	10	56	2002 Mar–2003 Aug
Lovell	235	1, 4	20	3	1984 Sep–1987 Dec
Lovell	325	8	10	2	1995 Feb–1996 Mar
Lovell	410	1, 2, 4, 8	10	54	1984 Sep–1997 Sep
Lovell	610	1, 4, 8	10	70	1984 Sep–2007 Oct
Lovell	925	8	10	6	1989 Feb–1989 Aug
Lovell	1400	32, 40, 96	10	410	1984 Aug–2009 Aug
Lovell	1520	384	5	128	2009 Aug–2017 Feb
Lovell	1625	32, 40	10	11	1989 Feb–1994 Nov
Goldstone DSS 13, 14	2388	12	>5	118	1969 Dec–1982 May

[a] TOAs were not calculated for these observations

Jodrell Bank observations were processed following Gould & Lyne (1998) for early observations and Hobbs et al. (2004) for more recent observations. A single pulse profile and one TOA were obtained for each observation. We omitted radio frequency interference (RFI)-contaminated profiles by visual inspection. Only those pulse profiles obtained during the LOFAR campaign have been used in this study. We processed the LOFAR observations using the PSRCHIVE[2] software library (Hotan, van Straten & Manchester 2004; van Straten, Demorest & Oslowski 2012). All the programs mentioned in the following paragraph are part of this package unless indicated otherwise. As a first step, we mitigated RFI present in the data sets using both PAZ and CLEAN.PY offered by the COAST GUARD package[3] (Lazarus et al. 2016). Subsequently, we folded each data set using an initial timing solution obtained by Hobbs et al. (2004). Small DM variations on time-scales of days can be non-negligible at these low frequencies. Therefore, we initially calculated the best DM value for each observation by maximizing the integrated pulse profile's signal-to-noise ratio (S/N) using PDMP. One total-intensity profile was obtained from each LOFAR observation. For each LOFAR station, we used one template of the pulse profile for each group of observations at the same frequency. The templates were obtained by fitting the main peak of a high S/N profile with a single von Mises function using PAAS. A TOA for each profile was calculated using PAT. Highly precise DM values were calculated from observations performed with the core and German stations using frequency-resolved timing. The details of this analysis are described in our companion paper by Donner et al. (in preparation), and the resulting DM time series is replicated in Fig. 2(a). These DM values

were applied in our work to correct for the time-variable dispersion both in our profile-shape investigations and in our long-term timing analysis. TOAs were not calculated for early commissioning and problematic observations (e.g. affected by strong interference or by software failures). In order to study the pulsar's profile evolution, the baseline was subtracted from each profile, and each profile was normalized to a peak amplitude of unity. Pulse profiles were aligned by cross-correlating the main peak with one single-peaked template.

The 15-min observation reported by Pilia et al. (2016) has been used extensively in this study. It is the first high-quality LOFAR observation available, dating back to 2011 October 24, and (coincidentally) was recorded almost simultaneously with the one known rotational glitch of PSR B2217+47 (Espinoza et al. 2011). This observation has a central frequency of 143 MHz and a bandwidth of 47 MHz divided into 3840 channels. It shows the transient component well separated from the main peak. It is also one of the few observations for which we have single-pulse data.

3 DATA ANALYSIS AND RESULTS

3.1 Timing analysis

All available TOAs have been fitted using TEMPO2[4] (Hobbs, Edwards & Manchester 2006) to refine the timing model. TOAs before Modified Julian Date (MJD) 45095 are from the NASA Deep Space Network and show an additional scatter in their residuals that is much larger than the quoted statistical uncertainties. To account for (the assumed) systematics in the data, we assigned these TOAs an equal uncertainty of 1 ms estimated from the scatter of their values.

[2] psrchive.sourceforge.net
[3] github.com/plazar/coast_guard

[4] bitbucket.org/psrsoft/tempo2

Table 2. Ephemeris obtained for PSR B2217+47. Uncertainties in parentheses refer to the last quoted digits.

Parameter	Value
Right ascension RA (J2000) (h:m:s)	22:19:48.128(4)
Declination DEC (J2000) ($^\circ$:$'$:$''$)	+47:54:53.82(4)
RA Proper Motion (mas yr^{-1})	$-12(3)$
DEC Proper Motion (mas yr^{-1})	$-19(3)$
Position Epoch (MJD)	49195
Spin period P (s)	0.538 469 450 53(2)
Spin period derivative $\dot{P}$ (10^{-15})	2.76516(6)
Spin frequency ν (Hz)	1.857 115 568 96(7)
Spin frequency derivative $\dot{\nu}$ (10^{-15} s^{-2})	$-9.5367(2)$
Period Epoch (MJD)	49195
DM (pc cm^{-3})	43.517(3)
DM Epoch (MJD)	49195
Glitch Epoch (MJD)	55859.43^a
Glitch $\Delta\nu$ (10^{-9} Hz)	2.15(2)
Glitch $\Delta\dot{\nu}$ (10^{-18} s^{-2})	$-5(1)$
Range of observations (MJD)	40585 − 57806
Surface magnetic field B (G)	1.2×10^{12}
Characteristic age τ (Myr)	3.1
Spin-down energy $\dot{E}$ (erg s^{-1})	7.0×10^{32}

^{a}Value from Espinoza et al. (2011).

The strong timing noise complicated a global fit. For this reason, we used the Cholesky method presented by Coles et al. (2011) to whiten the spectrum. We included in our model the one known rotational glitch of the pulsar (Espinoza et al. 2011). The parameters obtained from this fit are presented in Table 2, and the timing residuals are shown in Fig. 1(a). The residuals show a slow modulation over the considered timespan, compatible with the analysis presented by Cordes & Helfand (1980), Hobbs et al. (2010), and Shabanova, Pugachev & Lapaev (2013).

It was possible to verify the accuracy of our timing analysis using an independent measurement of the source position obtained from an imaging observation with the Very Long Baseline Array (VLBA) from the PSRπ pulsar astrometry campaign (Deller et al. 2011). Assuming an error dominated by systematic uncertainties on the position of PSR B2217+47 of 5 mas (Deller et al. 2016), the obtained right ascension is $22^h19^m48\overset{s}{.}1070(5)$ and the declination is $+47^\circ54'53.471(5)''$ on MJD 55569, consistent with the timing analysis after accounting for the measured proper motion.

In order to investigate a possible connection between the spin-down ($\dot{\nu}$) evolution of this pulsar and its pulse-shape variations, we used the method developed by Brook et al. (2016) to compute $\dot{\nu}(t)$. This method uses Gaussian Process Regression (GPR) to model timing residuals and profile variations. We found that the residuals of PSR B2217+47 were best fitted by a single squared exponential kernel (Rasmussen & Williams 2006) chosen due to its differentiable properties. To allow for uncertainty on the residuals, we used an additional white noise kernel. The fit is applied to the residuals by optimizing the hyperparameters $\theta(\lambda, \sigma^2, \sigma_n^2)$ associated with the kernels, where λ is the function smoothness, σ^2 is the average distance of the function from its mean value, and σ_n^2 specifies the noise variance. The optimized hyperparameters were $\lambda = 1000$ d, $\sigma^2 = 1.4 \times 10^{-4}$ s, and $\sigma_n^2 = 2.1 \times 10^{-7}$ s. The resulting spin-down evolution is shown in Fig. 1(b), where oscillations are visible on time-scales of the order of 3 yr. We find that the overall trend is approximately constant with a peak-to-peak fractional amplitude $\Delta\dot{\nu}/\dot{\nu} < 0.1$ per cent. The low quality of early TOAs did not permit to perform the analysis before 1988.

3.2 DM and flux variations

In our companion paper (Donner et al., in preparation), we present dramatic variations in the DM towards this pulsar, as measured
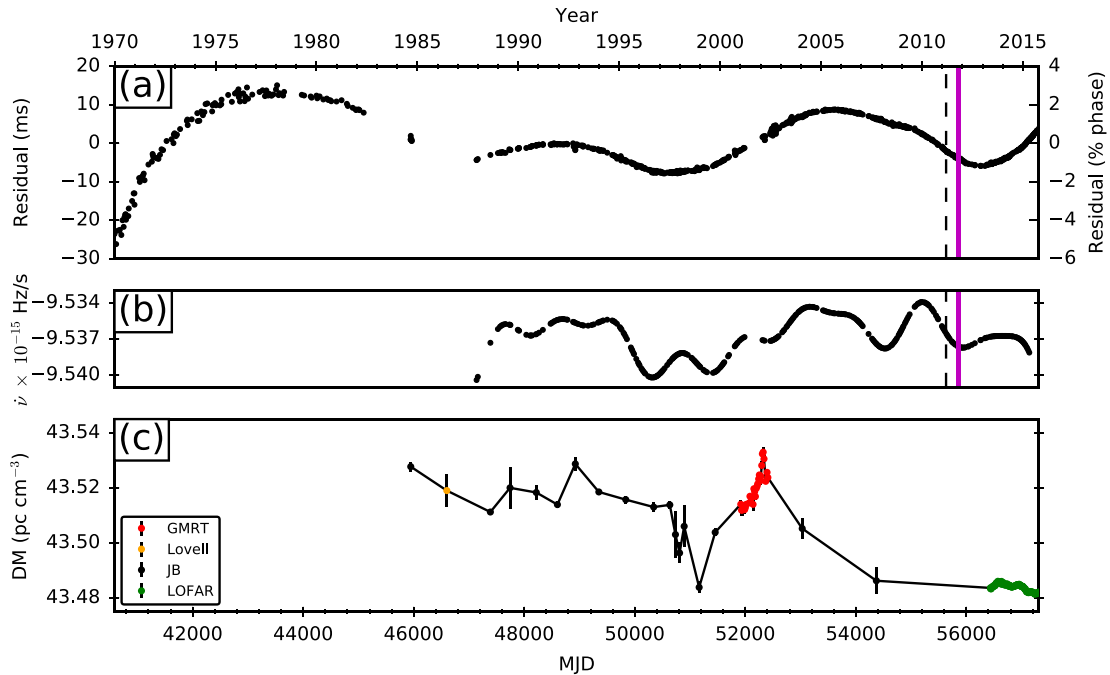

Figure 1. Residuals of the fit for the timing model reported in Table 2 (a) and spin-down variations (b). For both panels, the vertical dashed line indicates the first LOFAR observation and the vertical magenta line indicates the epoch of a rotational glitch. Long-term DM variations for the source are shown in panel c. Giant Metrewave Radio Telescope (GMRT) values (red) are from Ahuja et al. (2005) and the orange point was obtained by Hobbs et al. (2004) using the Lovell telescope. Black and green points are unpublished values from Jodrell Bank (JB) and LOFAR (core and German stations), respectively.
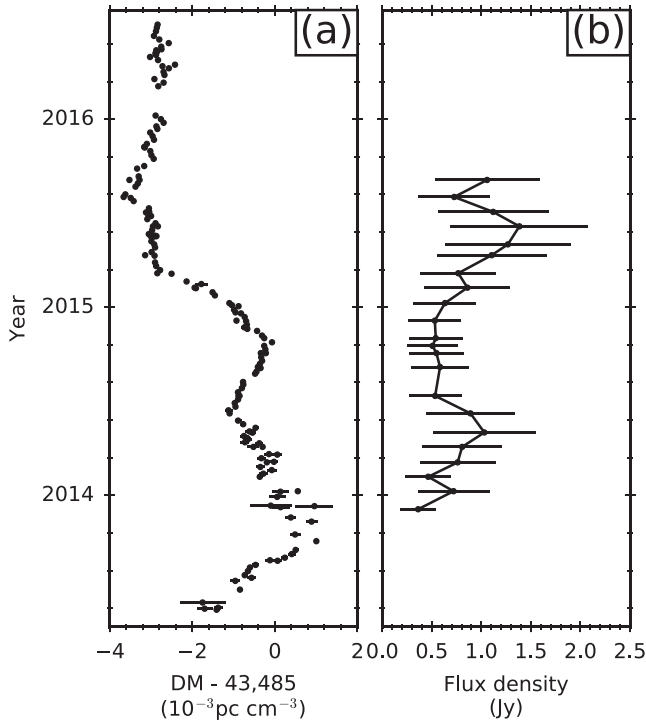
Figure 2. Panel a: DM of PSR B2217+47 measured by LOFAR, and panel b: mean flux density of PSR B2217+47 measured by LOFAR. 1σ error bars are often smaller than the points in panel (a), which is adapted from Donner et al. (in preparation).

from the LOFAR data taken with the international stations in Germany (i.e. the German Long Wavelength Consortium, GLOW). In Fig. 1(c), these DM values are plotted together with archival Lovell data (see Table 1 for details), and other published values.[5] DM variations obtained from GLOW and LOFAR core observations are further highlighted in Fig. 2(a). The level of DM variations derived from LOFAR data is $\sim 5 \times 10^{-3}$ pc cm^{-3}, roughly an order of magnitude lower than that reported by Ahuja et al. (2005). However, they are still significant compared to more typical DM variations observed along other lines of sight (e.g. Keith et al. 2013, and references therein).

A total of 23 observations obtained from the LOFAR core were suitable for flux and polarization calibration. We followed the procedure described in detail by Noutsos et al. (2015) and Kondratiev et al. (2016). The uncertainties of the resulting flux densities are conservatively estimated to be 50 per cent (Bilous et al. 2016). The resulting values are plotted in Fig. 2(b). Flux densities of recent Lovell observations are reported in Fig. 3(a). The scatter of data points is due to scintillation.

3.3 Pulse profile evolution

The evolution of the pulse profile in LOFAR observations is shown in Fig. 4. It is very complex, with different components evolving over months, but all *trailing* the main peak. The profile evolution can be divided into two different parts, where the transient component has different characteristics.

---

[5] Stovall et al. (2015) reported a significantly different DM value using LWA1. We attribute this offset to the strong scattering of the pulsar at 50 MHz.
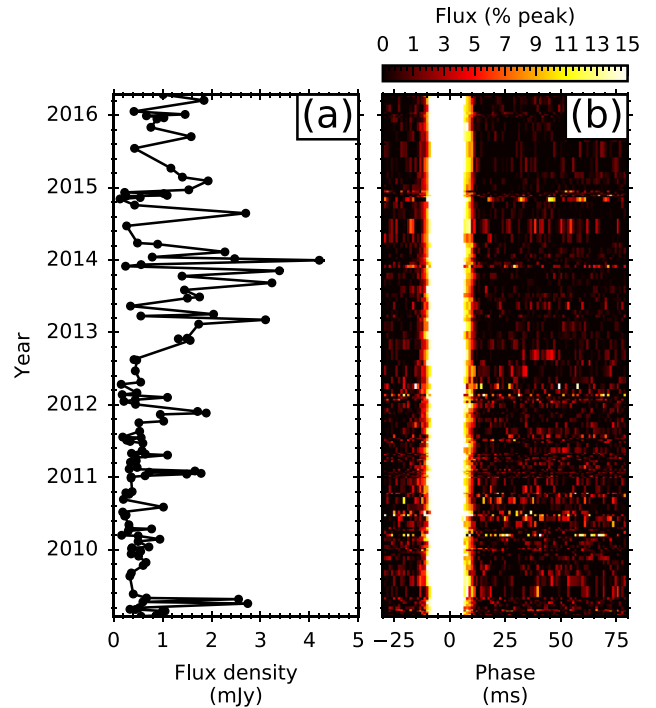

Figure 3. Panel a: mean flux density, and panel b: pulse profiles of PSR B2217+47 measured at 1.5 GHz by the Lovell telescope. All the profiles are normalized to a peak flux of unity and aligned by cross-correlating with a standard template (and saturated to 15 per cent of the peak intensity). 1σ error bars are often smaller than the points in panel (a).

(i) In early observations, a relatively bright component is present. It shifts towards the main peak until they overlap, reaching the closest approach in 2015.

(ii) A weaker component with a more complex structure brightens in 2014 and evolves with different characteristics, as highlighted in Fig. 4(b).

The low S/N and complex profile do not permit a robust model of the weaker component (ii). Therefore, component (i) was used in most of the analyses and we refer to it as the 'bright component'. None of these transient components is detectable in pulse profiles obtained at 1.5 GHz during the same period using the Lovell telescope (Fig. 3b), even when using the sensitive GPR method described by Brook et al. (2016).

Furthermore, we detected a weak precursor in LOFAR observations, visible in Fig. 4(b), which has not previously been reported in the literature. It is present during the whole observational campaign and does not seem to evolve in time. Therefore, it is likely intrinsic to the (low-frequency) pulsar profile but too weak for previous detection.

3.3.1 Frequency structure

In order to study the relative DM value of the transient component and its spectral index, we analysed its evolution as a function of observing frequency. The observation taken by Pilia et al. (2016) has been used because in this early observation the trailing component is relatively bright and well separated from the main peak compared to the situation in later observations. We manually defined two regions in the pulse profile for the transient component and the main peak, respectively.
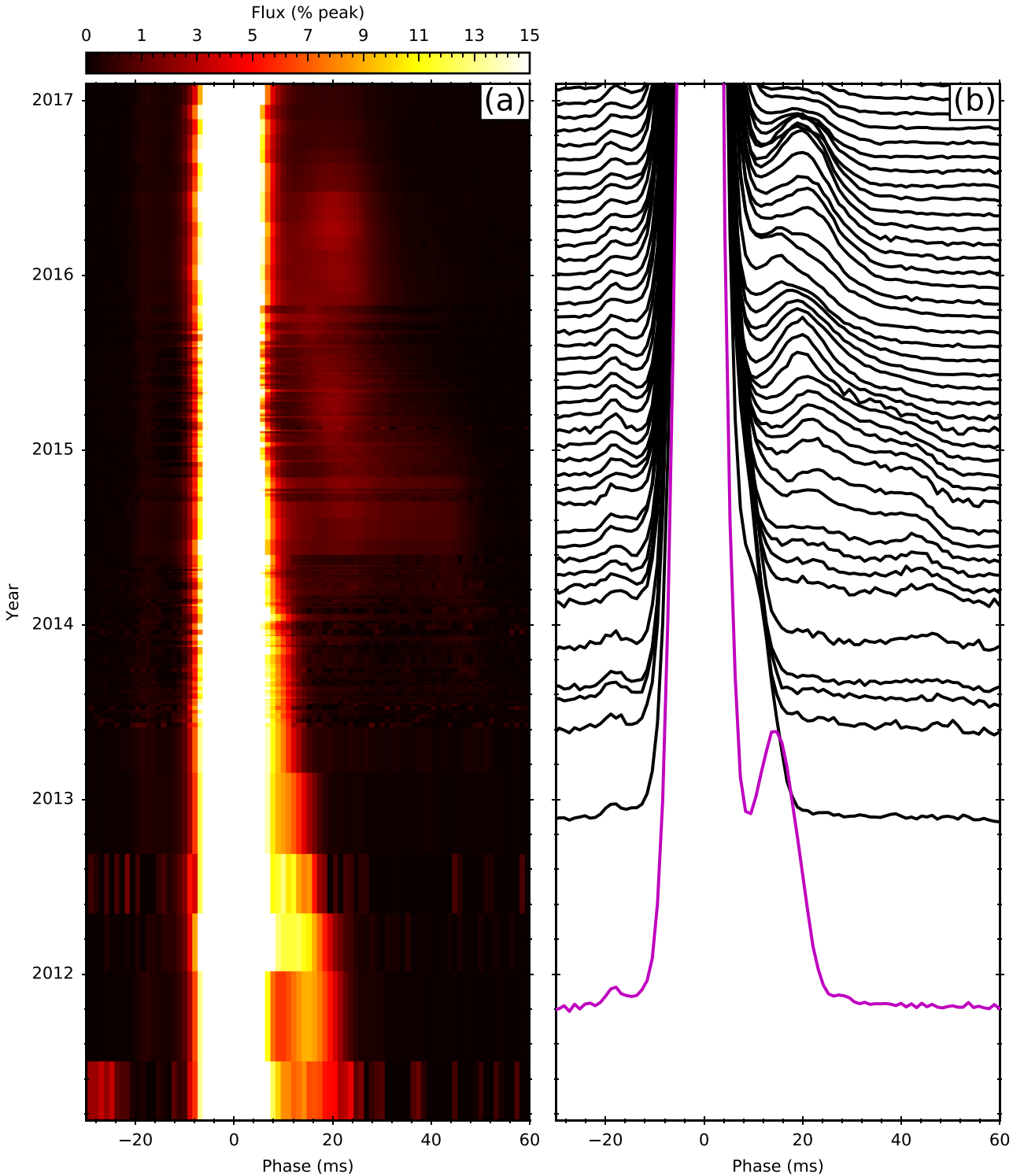
Figure 4. Profile evolution of PSR B2217+47 at 150 MHz during the 6-yr LOFAR observing campaign. All the profiles are normalized to a peak flux of unity and aligned by cross-correlating with a standard template. LOFAR was in a test phase until 2013 and observed with lower cadence and sensitivity. In panel (a), the profiles are saturated to 15 per cent of the peak intensity. Panel (b) highlights the complex profile evolution, with profiles averaged every 30 d and only those with S/N > 1000 included. The magenta profile is from Pilia et al. (2016).

The DM values of the two profile components have been analysed independently. Their partial overlap did not permit robust and independent cross-correlations with standard templates in each frequency channel. For this reason, we considered the peak position of the two components in each frequency channel.

A total of 2948 frequency channels contained both components brighter than three times the noise level. Considering an uncertainty of one phase bin, a fit to the frequency structure of the two components gave a statistically insignificant DM difference $\Delta DM = (3.9 \pm 7.0) \times 10^{-3} \, \text{pc cm}^{-3}$.

In order to obtain the spectral index of the transient component, we first calculated its spectral index relative to the main peak. The integrated flux of the two profile components was calculated for each frequency channel. We then considered the ratio between them so as to remove frequency structures due to the telescope response function, scintillation, RFI, etc. A fit of these values in different frequency channels gave a relative spectral index of the transient component with respect to the main peak of $\alpha_{rel} = -1.60 \pm 0.03$. Bilous et al. (2016) used LOFAR measurements together with multifrequency values from the literature to obtain a spectral index for the main component of PSR B2217+47 of $\alpha_{main} = -1.98 \pm 0.09$. Therefore, assuming no spectral turnover, the spectral index of the trailing component can be found using $\alpha_{transient} = \alpha_{main} + \alpha_{rel} = -3.58 \pm 0.09$.

The integrated flux of the transient component is 12 per cent that of the main peak at 150 MHz. Assuming constant values for the obtained spectral indices, these imply a ratio between the two components of 0.3 per cent at 1520 MHz. Since the pulsar is detected with S/N ~ 100 in typical Lovell observations, this steep spectrum explains the lack of detection of the transient component with Lovell.

We repeated the calculation in order to obtain the spectral index of the weaker transient component using 15 high-quality observations where it was relatively well separated from the main peak. These observations were recorded between 2014 October 4 and 2016 May 5. The average value of the spectral indices is $\alpha_{transient} = -3.73 \pm 0.06$, with all the 15 single values within 2σ from the average. This value is compatible with the spectral index of the bright transient component.

3.3.2 Single-pulse analysis

We studied the properties of single pulses from PSR B2217+47 using the observation reported by Pilia et al. (2016). It includes 1769 single pulses from the pulsar. We found a strong correlation between the flux density of the main peak and of the bright transient component in the individual single pulses detected in the observation (Fig. 5), with a Pearson correlation coefficient of 0.97. In order to test this result, we tried the same analysis on components belonging to adjacent single pulses, i.e. correlating the flux density of the transient component in each pulse with the flux density of the main peak in the next pulse. The correlation disappeared in this additional analysis. The slight deviation from a linear fit of the points visible in Fig. 5 may indicate a second-order effect or could be instrumental in origin.

3.3.3 Polarization measurements

The same LOFAR observations used to calculate flux densities in Section 3.2 were used to study polarization properties. One of the observations was taken at an earlier epoch and was excluded from the plots for clarity. Fig. 6(a) shows the polarization angle (PA) curves. Since a reference polarized signal was not used, an absolute polarization calibration was not possible to achieve. Therefore, PA curves were rotated to align at an arbitrary point in the middle of the plot in order to study the relative slope. Fig. 6(b) reports the pulse profiles obtained from the same observations for total intensity and linear polarization. The obtained profiles are compatible with those reported in Noutsos et al. (2015).

A random scatter of the values can be observed along the PA curves in Fig. 6(a), except for a specific area in the trailing edge
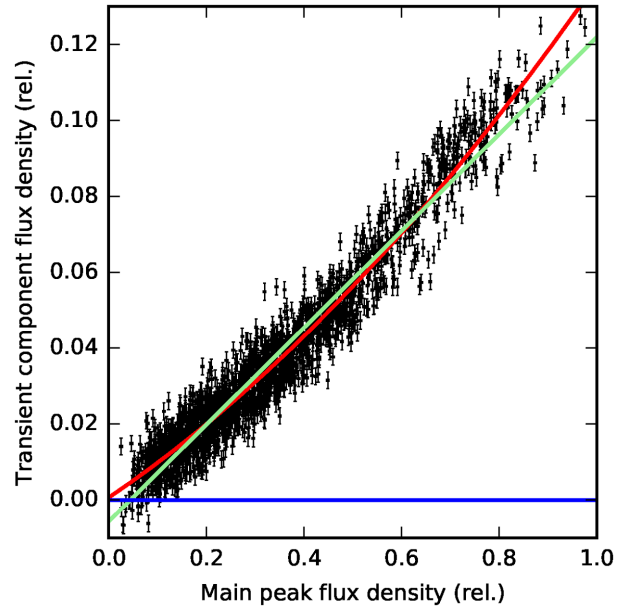

Figure 5. Scatter plot of the flux density of the transient component and main pulse peak in each single pulse of a 15-min LOFAR observation. Units are relative to the brightest pulse peak. The green and red lines are linear and quadratic fits to the points, respectively. The horizontal blue line represents the null flux density for the transient component and the points below are due to noise oscillations.

of the main peak, which approximately corresponds to the position of the brighter transient component. A higher flux of the transient component corresponds to a lower PA value in this region. In addition, the linear polarization fraction (L/I) across the profile does not evolve significantly in time. The leading part of the profile shows L/I ~ 50 per cent, whereas in the rest of the profile L/I ~ 20 per cent.

4 DISCUSSION

It is possible that cases of pulse profile evolution are fairly common among pulsars but are subtle and therefore difficult to observe. Pulse profile evolution could be magnified at lower frequencies where it may be detected in bright pulsars and with sensitive telescopes, as in our case. This hypothesis can be tested by regular monitoring of bright pulsars and will be further verified by the next generation of sensitive radio telescopes, in particular the Square Kilometre Array (SKA, Han et al. 2015).

Here, we consider three effects to explain the observed long-term evolution of PSR B2217+47's average pulse profile: (i) a change in the viewing geometry due to pulsar precession (as considered by Suleymanova & Shitov 1994), (ii) an intrinsic variation in pulsar emission related to changes in the magnetosphere (similar to those found for a sample of pulsars by Lyne et al. 2010), or (iii) variations due to intervening structures in the IISM (perhaps similar to the pulse echoes seen in the Crab pulsar, and associated with filaments in its surrounding nebula, by Backer et al. 2000; Lyne et al. 2001).

4.1 Pulsar precession

A smooth profile evolution is expected from precession due to the variation of viewing angle towards the magnetic axis and pulsar beam (Cordes 1993). Also, two different effects contribute to timing noise: the additional pulsar spin induced by precession and the
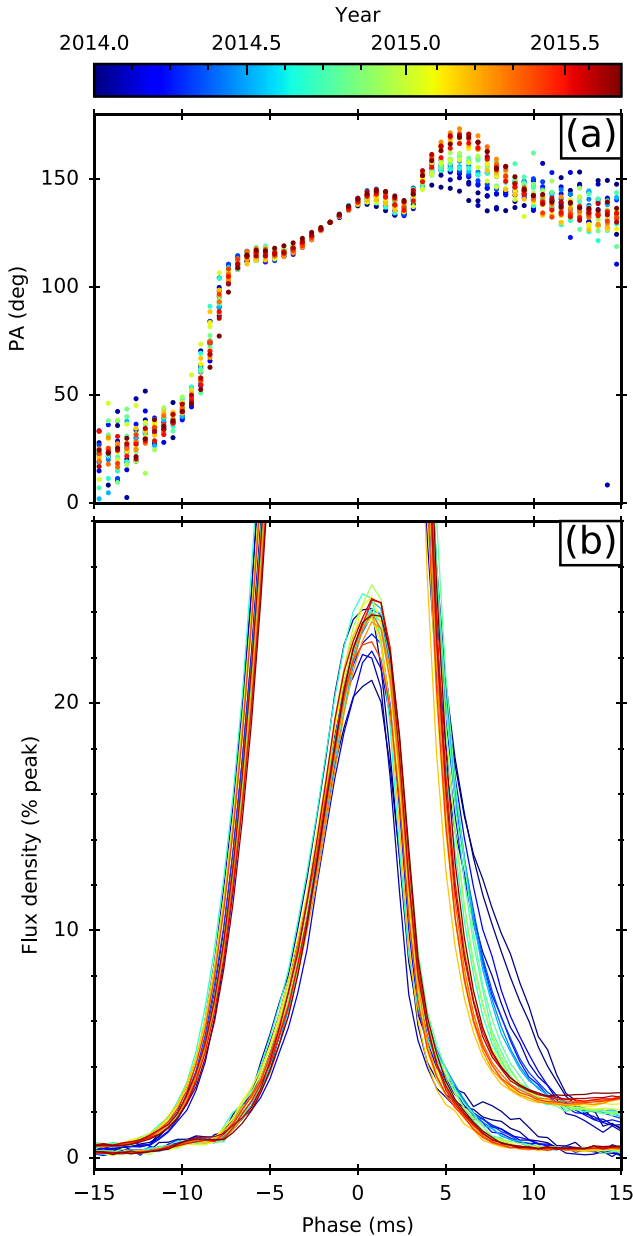
Figure 6. Evolution of the polarization properties of PSR B2217+47. PA curves are shown in panel (a). Pulse profiles of total intensity (brighter profiles) and linear polarization (weaker profiles) are shown in panel (b). The profiles have been normalized to the peak value of the total intensity for each observation. The colour scale indicates the epoch of the observations.

fluctuation of the torque due to the change in the angle between the spin and magnetic axes (Cordes 1993). In principle, pulsar precession could be a good explanation both for the structure of the timing residuals (timing noise) reported in Fig. 1(a) and for the smooth evolution of the average pulse profile shown in Fig. 4. However, the two effects happen on very different time-scales, and, thus, they are difficult to attribute to the same precession period, even if non-axisymmetric precession of the neutron star is present. Furthermore, the precession model does not explain the strong DM variations we detect, which would then be coincidental. Given the paucity in the literature of DM variations having the measured intensity in this short period, such a coincidence seems unlikely. In addition, all the observed profile variations only affect the trailing part of the profile,

whereas the shape and relative position of the weak precursor and the main peak are steady. This would be an additional coincidence in this scenario. Moreover, this model does not explain the correlation between the flux density of the main peak and of the bright transient component found in Section 3.3.2.

4.2 Variations in pulsar emission

Perturbations in the plasma filling the magnetosphere can cause a variation both in the average pulse profile (due to changes in particle flux and currents) and in the spin-down evolution of the neutron star (due to changes in the electromagnetic torque, Spitkovsky 2004; Kramer et al. 2006; Lyne et al. 2010). It is unclear whether the spin-down variations that we measure for PSR B2217+47 and reported in Fig. 1(b) are related with the observed profile variations visible in Fig. 4. However, a model with two or three separate $\dot{\nu}$ levels as proposed by Lyne et al. (2010) is clearly inconsistent with our results.

Three models possibly related to changes in the pulsar's magnetosphere were considered, namely the nested cone model (Rankin 1983), the refractive model (Barnard & Arons 1986), and an asteroid encounter (Cordes & Shannon 2008), but none of these models readily explain the observed asymmetry in the pulse profile evolution, the strong DM variations detected, or the correlation found between the flux density of the main peak and of the transient component.

4.2.1 The role of the glitch

A connection between pulse profile variations and spin-down evolution has been observed by Weltevrede, Johnston & Espinoza (2011) in PSR J1119−6127, where a temporary change in the pulse profile was contemporaneous with, and thus likely induced by, a glitch in the pulsar's rotation. The connection is interesting to consider in light of the glitch detected in close proximity to the Pilia et al. (2016) observation. However, the profile of PSR J1119−6127 changed on a weekly time-scale as opposed to the yearly variations observed in PSR B2217+47. An analysis of the pulse profile evolution in PSR B2217+47 shows that the occurrence of the glitch only coincides with a large separation between the bright transient component and the main pulse, but transient profile components were also detectable before the glitch occurred.

Weltevrede et al. (2011) also detected a few strong pulses from PSR J1119−6127, at a particular pulse phase where no components were present in the integrated pulse profile, in the first single-pulse resolved observation after the glitch. We performed a search for bright single pulses away from the profile components in the LO-FAR observation presented by Pilia et al. (2016). We did not find any pulse above 6 per cent of peak intensity in that observation before a phase of −0.05 or after a phase of 0.04 with respect the main peak.

4.3 Structures in the IISM

A structure in the IISM close to the LoS could create an additional transient component in the pulse profile by deflecting radio waves back to the observer. The leading edge of the profile is expected to be unaffected by IISM propagation, as is observed in all the profile variations detected in PSR B2217+47 (including the one reported by Suleymanova & Shitov 1994). This is a firm prediction to test this hypothesis with future observations.

The transient component will have a delay with respect to the direct signal, and its evolution with time is analysed in Appendix A.
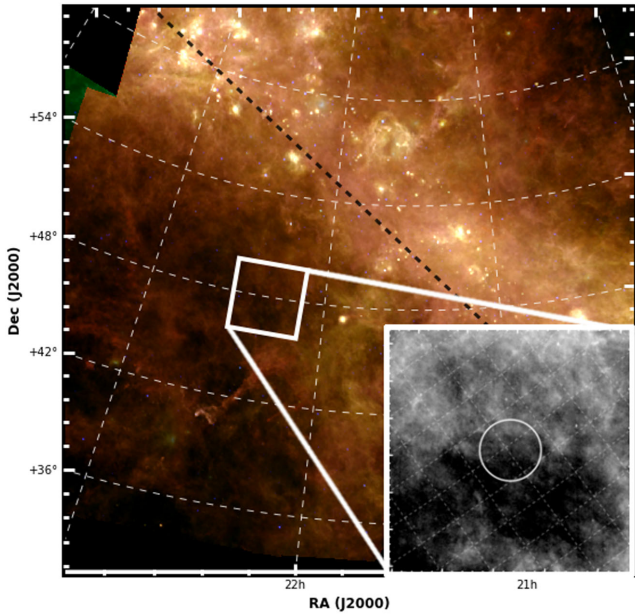
Figure 7. A three colour mosaic of images of the field around PSR B2217+47 (Miville-Deschênes & Lagache 2006) obtained with the *Infrared Astronomical Satellite (IRAS)* through the Improved Reprocessing of the IRAS Survey (IRIS). Red is the 100 μm band, green is the 60 μm band, and blue is the 25 μm band. The dashed black line indicates the Galactic Plane. The inset is a 60 μm *AKARI* observation (Murakami et al. 2007). The white circle is centred on the pulsar location and has a radius of 30 arcsec. The white box and *AKARI* image are 4 × 4 arcmin².

Figure 8. Comparison between panel a: the profile evolution of PSR B2217+47 and panel b: of the Crab pulsar (b, Lyne et al. 2001). The profiles in panel (a) are clipped between 5 per cent and 15 per cent of the peak intensity, interpolated with a linear spline and plotted with a logarithmic colour scale to highlight the evolution of the brightest transient component.

In most of the practical cases, this evolution will be quadratic in time (equation A4). Despite the fact that only the bright transient component could be analysed in detail, it is plausible to assume that the multiple transient components observed have the same origin. In the IISM interpretation, they could arise from a group of structures or from inhomogeneities in a large structure passing close to the LoS. Since the scattering process is highly chromatic, the steep spectrum of the transient components is also expected within this model. The strong DM variations presented in Figs 1(c) and 2(a) prove that there is significant variability in the IISM towards this pulsar and the same IISM structures can explain both the effects. A strong support to this model is given by the correlation in single pulses between the flux density of the bright transient component and the main peak discussed in Section 3.3.2. This is also expected if the transient component is an echo of the main peak.

Fig. 7 shows an infrared image of the field of PSR B2217+47. Clouds of dust and gas are seen to extend from the Galactic plane. This is thus an inhomogeneous region of the neutral interstellar medium where ionized structures could possibly form. On the contrary, there is no clear indication of a bright, compact structure near the pulsar. Also, no obvious structure is visible in the H α map presented by Finkbeiner (2003). X-ray images of the field obtained by *ROSAT* (Voges et al. 1999) do not show any significant emission from the pulsar region either.

An echo in a pulsar's pulse profile has previously been observed in PSR B0531+21 (Backer et al. 2000; Lyne et al. 2001), although in that case the structures are believed to be within the Crab nebula itself and not the IISM. Fig. 8 shows a visual comparison between the evolution of the bright transient component in PSR B2217+47 and a Crab echo event reported by Lyne et al. (2001). The evolution of the two transient components presents some similarities.
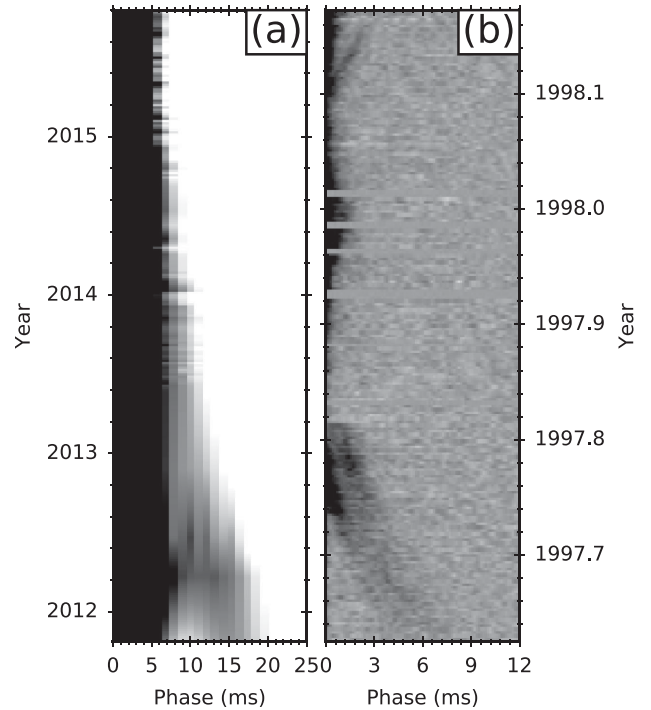
The feature in the Crab shows a parabolic shape in time versus rotational phase (as expected from equation A4), and the separation of the component in PSR B2217+47 seems consistent with such an approach, although the S/N and number of observations in the earlier eras are insufficient to precisely quantify this. Also, the relative fractional power in the transient components is of the same order in the two cases, between ∼5 per cent and 10 per cent of the integrated pulse flux. The different time-scales of the two evolutionary paths can be ascribed to different relative distances between the structure, pulsar, and Earth (equation A4). The absence of a symmetric receding arm in the evolution of the bright transient component of PSR B2217+47 may be due to a non-spherical geometry of the IISM structure (e.g. elongated in one or two directions). About 30 per cent of the Crab echoes reported by Lyne et al. (2001) only show one of the parabolic arms. It is interesting to note that Osłowski et al. (in preparation) observe with LOFAR a low-frequency profile evolution of PSR B1508+55 that presents various similarities to the one reported here. Three transient components appear at different epochs and shift quadratically in phase over years with the original detection corresponding to a much larger delay than presented here. They also attribute the evolution to IISM effects.

The IISM model cannot entirely account for the strong timing noise observed in PSR B2217+47. Despite the fact that small profile variations can cause timing noise (e.g. Lentati et al. 2017), most of the timing observations used here were acquired around 1.5 GHz, where the flux inferred for the transient component is less than 0.3 per cent of the main pulse, and a GPR analysis found no evidence for profile variability (Section 3.3). In addition, the peak-to-peak variations in the timing residuals is ∼30 ms compared to a main component width of ∼8 ms at 1.5 GHz. Furthermore, the presence of timing noise in many slow-spinning pulsars (Cordes &

Helfand 1980; Hobbs et al. 2004) supports the hypothesis that the two effects are unrelated.

5 MODELLING THE IISM STRUCTURE

Among the three interpretations we considered in the previous section, the IISM model is the one that best explains the characteristics of the observed profile evolution of PSR B2217+47. Here, we use the observations to infer some properties of the IISM structure possibly causing the profile evolution. We calculate a distance to the structure from Earth by using equation (A7) and the separation in pulse phase of the bright transient component (Fig. 4). Around $t = 3.5 \pm 0.3$ yr before the closest approach, the delay of the transient component is $\tau = 14.5 \pm 0.5$ ms. The overlap with the main peak suggests that the IISM structure nearly crosses the LoS, with a delay $\tau_* = 1 \pm 1$ ms. The timing solution presented in Table 2 implies a pulsar proper motion $\mu = 20.6 \pm 2.9$ mas yr^{-1}, and the pulsar distance is estimated to be $r = 2.2 \pm 0.3$ kpc using the NE2001 model (Cordes & Lazio 2002). The proper motion of the IISM structure is assumed to be negligible since the pulsar speed is estimated to be much larger than typical IISM velocities (e.g. Hill et al. 2005) and the Earth's orbital speed. From equation (A7), the resulting distance of the IISM structure from Earth is $d = 1.1 \pm 0.2$ kpc, approximately half the pulsar distance. The error is dominated by the uncertainty on the pulsar's proper motion. The distance of the structure implies a deflection angle $\delta = 150 \pm 25$ mas.

We estimated the transverse radius of the IISM structure that causes the DM variation detected by LOFAR:

$$R \approx d\mu t, \tag{1}$$

where t in this case is the timespan during which the variation is present. Fig. 2(a) shows the density profile of the IISM causing the DM variation along the axis parallel to the pulsar's transverse velocity. The exact structures causing the DM and profile variation may not be the same, but are likely to belong to the same group, i.e. to be close in space with respect to the relative distances of the pulsar, IISM structure, and Earth. Therefore, we can substitute the distance from the IISM structure calculated above. The largest DM variation in LOFAR data lasts for $t \gtrsim 1.5$ yr, which implies $R \gtrsim 34$ au. Under the assumption that the system scale does not change significantly in two decades, we can repeat the calculation for the DM variation reported by Ahuja et al. (2005). Considering the bulk of the DM variation to last for $t \approx 400$ d, we obtain $R \approx 25$ au. The observed DM variations imply that most of the IISM structures are overdense, in agreement with Romani, Blandford & Cordes (1987) and Bannister et al. (2016), and in contrast to Pen & King (2012), although one underdense region is apparent in Fig. 1(c) around MJD 51000, right before the DM variation reported by Ahuja et al. (2005).

5.1 Ionized blobs

We consider the possibility that the observed profile variations are due to deflection by approximately axially symmetric IISM structures (Walker & Wardle 1998). We calculate the implied electron density using both DM and profile variations. From the DM variation:

$$\Delta DM = L\bar{n}_e, \tag{2}$$

where $\bar{n}_e$ is the average electron density of the IISM structure and where L is the radius of the structure along the LoS. If we assume

spherical symmetry, $L \approx R$ and the relation can be combined with equation (1) to obtain

$$\bar{n}_e \approx \frac{\Delta DM}{d\mu t}. \tag{3}$$

From Fig. 2(a), we estimate $\Delta DM \approx 4 \times 10^{-3}$ pc cm^{-3}, which implies $\bar{n}_e \approx 25$ cm^{-3}. The same calculation for the DM variation reported by Ahuja et al. (2005), $\Delta DM \approx 0.02$ pc cm^{-3}, implies $\bar{n}_e \approx 170$ cm^{-3}.

Considering a refractive plasma lens, Hill et al. (2005) found the relation between the mean electron density of the lens $\bar{n}_e$ and the refracting angle δ:

$$\bar{n}_e = \frac{5.4\delta}{\lambda^2} \ \text{m}^2 \, \text{mas}^{-1} \, \text{cm}^{-3}, \tag{4}$$

where λ is the observing wavelength, which varies between ~1.5 and 2.5 m across the LOFAR HBA band. Substituting the values we calculated in the previous section, we find $\bar{n}_e \sim 130$–360 cm^{-3} across the band. This value is in good agreement with the mean electron density inferred from the DM variation reported by Ahuja et al. (2005). The obtained electron densities are roughly consistent with standard ESE models (e.g. Maitia, Lestrade & Cognard 2003; Hill et al. 2005).

5.2 IISM structures around hot stars

During the writing of this manuscript, Walker et al. (2017) presented evidence for ionized clouds around hot stars causing intra-day variability of radio quasar fluxes. If confirmed, the same structures could generate ESEs and explain the high electron density required. The distance estimated above for the IISM structure causing the profile variation of PSR B2217+47 is ~1 kpc, under the assumption that the pulsar proper motion is much higher than the proper motion of the structure. However, structures connected with a star will have approximately its same velocity, usually larger than the average speed of the interstellar medium (e.g. van Leeuwen 2007). Unfortunately, the large uncertainty in the distance estimated from equation (A7) does not permit to put constraints on the expected star's distance.

Following Walker et al. (2017), we searched for hot stars (spectral types O, B, and A) closer than 2 pc to PSR B2217+47's LoS in the *Hipparcos* catalogue (Perryman et al. 1997). Unfortunately, stellar spectra are not available at distances ≫100 pc. Only stars with a reliable parallax measurement (i.e. larger than the 2σ value) were selected. Three stars met these criteria, all with a spectral type A.

(i) HIP 110422 is at 101 ± 6 pc and ~1.9 pc from the LoS.
(ii) HIP 110253 is at 230 ± 30 pc and ~1.8 pc from the LoS.
(iii) HIP 110139 is at 350 ± 70 pc and ~1.8 pc from the LoS.

In order to evaluate the probability of coincident alignment, we considered a 15×15 deg^2 sky region centred on the pulsar position. A total of 387 hot stars were present in the catalogue in this area. Selecting 10^6 random positions in this area, we found that on average ~1 hot star was closer than 2 pc to the LoS, in agreement with Walker et al. (2017). We conclude that this is an interesting hypothesis but our data does not permit to constrain it.

5.3 Scintillation arcs and inclined sheet model

We considered the possibility that the observed profile variation is an effect similar to scintillation arcs. Similar IISM structures could in principle account for both effects. In fact, scintillation arcs

could be caused by structures closer to the LoS that deflect higher frequency radio waves at lower deflection angles. The delay of the deflected waves will be shorter and they will interfere with the direct waves. The same structures might deflect lower frequency waves at higher deflection angles when farther away from the LoS. In this case, the delay of the deflected waves will be longer and they will create additional components in the pulse profile, trailing the main peak.

Compared to blobs, corrugated plasma sheets that are nearly aligned with the LoS require a lower density to deflect radio waves at the required angle (Pen & Levin 2014). The same argument can be used in this study to explain the strong DM variations that were detected. Simard & Pen (2017) described a typical plasma density in the sheet on the order of $n_e = 0.3 \, \text{cm}^{-3}$. Substituting into equation (2), this implies a length $L = 10^4$ au from the DM variation reported by Ahuja et al. (2005) and $L = 3 \times 10^3$ au from the more recent DM variation measured with LOFAR. The radius $R \sim 30$ au calculated in the previous section would represent, in this scenario, the projected width of the sheets. It is unclear whether these values are in agreement with inclined sheet models.

6 CONCLUSIONS

We presented the analysis of pulse profile evolution of PSR B2217+47, similar to an event previously reported by Suleymanova & Shitov (1994). We performed an intensive, multiyear observing campaign with LOFAR ($\sim$150 MHz) and Lovell ($\sim$1.5 GHz) telescopes. A smooth but complex evolution of the pulse profile was observed during the entire duration of the LOFAR observing campaign. In addition, we report for the first time the presence of a weak precursor visible in LOFAR observations, which remains stable for the whole range of our observing campaign. No profile evolution was detected during the same timespan at 1.5 GHz with the Lovell telescope. Significant variations in the ionized interstellar electron density towards this pulsar are possibly related and are discussed in a companion paper (Donner et al., in preparation). An earlier episode of large interstellar density variations was reported by Ahuja et al. (2005).

Both pulsar precession, considered as a possible explanation for the observed profile evolution by Suleymanova & Shitov (1994), and an intrinsic variation in the pulsar emission do not explain the coincident DM variations, the stability of the leading edge of the profile, and a correlation between the flux density of the transient component and of the main peak in the single pulses of one observation. On the other hand, these characteristics can be attributed to propagation effects in the IISM. Also, there is evidence for a quadratic approach of the transient component to the main peak, which is expected in this model, although the quality and cadence of early observations do not permit a robust analysis. Future high-resolution images at 150 MHz could spatially resolve the IISM structure, and thereby confirm this interpretation. We inferred some of the properties of the putative IISM structures causing DM and profile variations and discussed the two main models to explain ESEs (Walker & Wardle 1998; Pen & King 2012) in this context in Sections 5.1 and 5.3.

Time-variable dispersion and profile-shape changes affect both the precision and accuracy of pulsar timing experiments (e.g. Cognard et al. 1993). IISM variations far less significant than those observed in PSR B2217+47 are already significantly affecting most of the currently existing high-precision pulsar-timing data sets (Verbiest et al. 2016). It is therefore a timely effort to investigate and characterize these events and to constrain their origins and occur-

rence rates, in order to allow their proper modelling and treatment in the decades to come.

REFERENCES

Ahuja A. L., Gupta Y., Mitra D., Kembhavi A. K., 2005, MNRAS, 357, 1013

Backer D. C., Wong T., Valanju J., 2000, ApJ, 543, 740

Bannister K. W., Stevens J., Tuntsov A. V., Walker M. A., Johnston S., Reynolds C., Bignall H., 2016, Science, 351, 354

Barnard J. J., Arons J., 1986, ApJ, 302, 138

Basu R., Mitra D., Rankin J. M., 2015, ApJ, 798, 105

Bilous A. V. et al., 2016, A&A, 591, A134

Brook P. R., Karastergiou A., Buchner S., Roberts S. J., Keith M. J., Johnston S., Shannon R. M., 2014, ApJ, 780, L31

Brook P. R., Karastergiou A., Johnston S., Kerr M., Shannon R. M., Roberts S. J., 2016, MNRAS, 456, 1374

Cognard I., Bourgois G., Lestrade J.-F., Biraud F., Aubry D., Darchy B., Drouhin J.-P., 1993, Nature, 366, 320

Coles W., Hobbs G., Champion D. J., Manchester R. N., Verbiest J. P. W., 2011, MNRAS, 418, 561

Cordes J. M., 1975, ApJ, 195, 193

Cordes J. M., 1993, in Phillips J. A., Thorsett S. E., Kulkarni S. R., eds, ASP Conf. Ser. Vol. 36, Planets Around Pulsars. Astron. Soc. Pac., San Francisco, p. 43

Cordes J. M., Helfand D. J., 1980, ApJ, 239, 640

Cordes J. M., Lazio T. J. W., 2002, preprint (arXiv:astro-ph/0207156)

Cordes J. M., Shannon R. M., 2008, ApJ, 682, 1152

Deller A. T. et al., 2011, in Alef W., Bernhart S., Nothnagel A., eds, 20th Meeting of the European VLBI Group for Geodesy and Astronomy p. 178 (arXiv:1110.1979)

Deller A. T. et al., 2016, ApJ, 828, 8

Downs G. S., Reichley P. E., 1983, ApJS, 53, 169

Espinoza C. M., Lyne A. G., Stappers B. W., Kramer M., 2011, MNRAS, 414, 1679

Fiedler R. L., Dennison B., Johnston K. J., Hewish A., 1987, Nature, 326, 675

Finkbeiner D. P., 2003, ApJS, 146, 407

Gould D. M., Lyne A. G., 1998, MNRAS, 301, 235

Graham Smith F., Lyne A. G., Jordan C., 2011, MNRAS, 410, 499

Han J. L. et al., 2015, Proc. Sci., Three-dimensional Tomography of the Galactic and Extragalactic Magnetoionic Medium with the SKA. SISSA, Trieste, PoS(AASKA14)041

Helfand D. J., Manchester R. N., Taylor J. H., 1975, ApJ, 198, 661

Hill A. S., Stinebring D. R., Asplund C. T., Berwick D. E., Everett W. B., Hinkel N. R., 2005, ApJ, 619, L171

Hobbs G., Lyne A. G., Kramer M., Martin C. E., Jordan C., 2004, MNRAS, 353, 1311

Hobbs G. B., Edwards R. T., Manchester R. N., 2006, MNRAS, 369, 655

Hobbs G., Lyne A. G., Kramer M., 2010, MNRAS, 402, 1027

Hotan A. W., van Straten W., Manchester R. N., 2004, PASA, 21, 302

Karastergiou A., Roberts S. J., Johnston S., Lee H., Weltevrede P., Kramer M., 2011, MNRAS, 415, 251

Keith M. J. et al. 2013, MNRAS, 429, 2161

Kondratiev V. I. et al., 2016, A&A, 585, A128

Kramer M., Lyne A. G., O'Brien J. T., Jordan C. A., Lorimer D. R., 2006, Science, 312, 549

Kuzmin A. D., Izvekova V. A., Shitov Y. P., Sieber W., Jessner A., Wielebinski R., Lyne A. G., Smith F. G., 1998, A&AS, 127, 355

Lazarus P., Karuppusamy R., Graikou E., Caballero R. N., Champion D. J., Lee K. J., Verbiest J. P. W., Kramer M., 2016, MNRAS, 458, 868

Lentati L., Kerr M., Dai S., Shannon R. M., Hobbs G., Osłowski S., 2017, MNRAS, 468, 1474

Liu K., Keane E. F., Lee K. J., Kramer M., Cordes J. M., Purver M. B., 2012, MNRAS, 420, 361

Lorimer D. R., Kramer M., 2004, Handbook of Pulsar Astronomy. Cambridge Univ. Press, Cambridge

Lyne A. G., Pritchard R. S., Graham-Smith F., 2001, MNRAS, 321, 67

Lyne A., Hobbs G., Kramer M., Stairs I., Stappers B., 2010, Science, 329, 408

Maitia V., Lestrade J.-F., Cognard I., 2003, ApJ, 582, 972

Manchester R. N., 2017, J. Phys., 932, 012002 (arXiv:1801.04318),

Mitra D., Rankin J. M., 2011, ApJ, 727, 92

Miville-Deschênes M.-A., Lagache G., 2006, in Armus L., Reach W. T., eds, ASP Conf. Ser. Vol. 357, The Spitzer Space Telescope: New Views of the Cosmos. Astron. Soc. Pac., San Francisco, p. 167

Murakami H. et al., 2007, PASJ, 59, S369

Noutsos A. et al. 2015, A&A, 576, A62

Pen U.-L., King L., 2012, MNRAS, 421, L132

Pen U.-L., Levin Y., 2014, MNRAS, 442, 3338

Perryman M. A. C. et al., 1997, A&A, 323, L49

Pilia M. et al., 2016, A&A, 586, A92

Rankin J. M., 1983, ApJ, 274, 333

Rasmussen C. E., Williams C. K. I., 2006, Gaussian Processes for Machine Learning

Rickett B. J., 1990, ARA&A, 28, 561

Romani R. W., Blandford R. D., Cordes J. M., 1987, Nature, 328, 324

Ruderman M. A., Sutherland P. G., 1975, ApJ, 196, 51

Shabanova T. V., Pugachev V. D., Lapaev K. A., 2013, ApJ, 775, 2

Shemar S. L., Lyne A. G., 1996, MNRAS, 282, 677

Simard D., Pen U.-L., 2017, preprint, (arXiv:1703.06855)

Spitkovsky A., 2004, in Camilo F., Gaensler B. M., eds, Proc. IAU Symp. Vol. 218, Young Neutron Stars and Their Environments. Astron. Soc. Pac., San Francisco, CA, p. 357 (astro-ph/0310731)

Stairs I. H., Lyne A. G., Shemar S. L., 2000, Nature, 406, 484

Stappers B. W. et al., 2011, A&A, 530, A80

Stinebring D. R., McLaughlin M. A., Cordes J. M., Becker K. M., Goodman J. E. E., Kramer M. A., Sheckard J. L., Smith C. T., 2001, ApJ, 549, L97

Stovall K. et al., 2015, ApJ, 808, 156

Suleymanova S. A., Shitov Y. P., 1994, ApJ, 422, L17

Taylor J. H., Huguenin G. R., 1969, Nature, 221, 816

Taylor G. B. et al., 2012, J. Astron. Instrum., 1, 1250004

Tingay S. J. et al., 2013, PASA, 30, e007

van Haarlem M. P. et al., 2013, A&A, 556, A2

van Leeuwen F., 2007, A&A, 474, 653

van Straten W., Demorest P., Oslowski S., 2012, Astron. Res. Technol., 9, 237

Verbiest J. P. W. et al., 2016, MNRAS, 458, 1267

Voges W. et al., 1999, A&A, 349, 389

Walker M., Wardle M., 1998, ApJ, 498, L125

Walker M. A., Tuntsov A. V., Bignall H., Reynolds C., Bannister K. W., Johnston S., Stevens J., Ravi V., 2017, ApJ, 843, 15

Weltevrede P., Johnston S., Espinoza C. M., 2011, MNRAS, 411, 1917

APPENDIX A: EVOLUTION OF THE TIME DELAY OF AN ECHO IN THE PULSE PROFILE

When a density change in the IISM deflects radio waves from a pulsar back to the LoS, an echo in the pulse profile may be detected. The delay between the echo and the normal components in the pulse profile is due to the additional path length. This is depicted in Fig. A1, where a pulsar is moving in the barycentric reference system with respect to a structure in the IISM. Although a blob of plasma is represented in the cartoon, this model accounts for any deflection that a structure in the IISM may produce. In fact, the discussion is based on geometrical considerations and does not depend on the proprieties of the IISM structure or of the deflecting mechanism. We calculate the distance d between the observer and the IISM structure by considering two values of the echo delay at different times. These are produced by different geometrical configurations of the system indicated with black and red colours in the illustration.
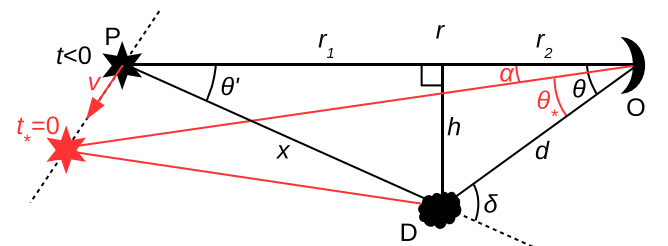

Figure A1. Schematic representation of the geometry causing an echo in the pulse profile (not to scale). A density variation in the IISM (D) deflects at an angle δ radio waves emitted from a pulsar (P) back to the observer (O). The pulsar is moving with a velocity v with respect to the IISM structure and thus the angles α, θ and θ' evolve with time. Two different epochs are represented: red symbols indicate the system configuration at the closest approach, i.e. when θ and θ' are smallest, whereas black symbols refer to an arbitrary time t ($t < 0$ in this example). The distance h of the LoS to the IISM structure divides the distance r from Earth to the pulsar in two segments r_1 and r_2. x is the distance between the pulsar and the IISM structure D.

In Fig. A1, the geometrical delay between direct and deflected radio waves is given by

$$\tau = \frac{d + x - r}{c}, \tag{A1}$$

where c represents the speed of light and the other quantities are defined in Fig. A1. Noting that $r = r_1 + r_2$, this can be rewritten as

$$\tau = \frac{x}{c}\left(1 - \cos\theta'\right) + \frac{d}{c}\left(1 - \cos\theta\right). \tag{A2}$$

In all practical cases, the angles θ and θ' are very small, therefore we can approximate the relation as

$$\tau \approx \frac{x\theta'^2 + d\theta^2}{2c}. \tag{A3}$$

In the small-angle approximation, the sine law gives $x\theta' = d\theta$, which, substituted in the previous equation, yields

$$\tau \approx \frac{\theta^2 d}{2c}\left(\frac{d}{x} + 1\right). \tag{A4}$$

In equation (A4), the only quantity changing in the considered timespan is θ. We can assume that θ evolves at a nearly constant rate given the short path travelled by the pulsar compared to the system scale. This implies a quadratic variation of the delay in time across the pulse profile.

To find the distance d as a function of τ and θ, we can substitute x with its expression from the cosine law, after applying the small-angle approximations. This, however, leads to a cubic equation in d difficult to invert. We calculate approximated equations considering three different configurations: (i) an IISM structure local to the pulsar, (ii) near half-way between the pulsar and the Earth, and (iii) local to the Earth. The delay can be expressed as

$$
\begin{aligned}
d \approx r &\quad\Rightarrow\quad \tau \approx \frac{r\theta^2}{2c}\left(\frac{r}{x} + 1\right) &\quad \text{local to pulsar,} \\
\theta \approx \theta' &\quad\Rightarrow\quad \tau \approx \frac{dr\theta^2}{2c(r-d)} &\quad \text{half} - \text{way,} \\
x \approx r &\quad\Rightarrow\quad \tau \approx \frac{d\theta^2}{2c}\left(\frac{d}{r} + 1\right) &\quad \text{local to Earth,}
\end{aligned}
\tag{A5}
$$

where we made use of the relations $r_1 = x\cos\theta'$ and $r_2 = d\cos\theta$ and ignored terms of higher order to obtain the relation for the half-way configuration.

The angle θ can be estimated by measuring delay values at two different epochs if one corresponds to the closest approach. We denote quantities measured at the closest approach with an asterisk.

The angle α can be expressed as $\alpha = \mu t$, where μ is the pulsar proper motion and t is the time between the two observation ($t_* = 0$). Since the triangle formed by the pulsar at the two epochs and the structure is right-angled, we obtain $\theta^2 = \theta_*^2 + \mu^2 t^2$. Evaluating equation (A4) for τ and τ_*, we get

$$\theta = \mu t\sqrt{\frac{\tau}{\tau - \tau_*}}. \tag{A6}$$

For structures that cross the LoS, $\tau_* = 0$ and hence equation (A6) reduces to $\theta = \mu t$.

By inverting equations (A5) and substituting equation (A6), we obtain

$$
\begin{aligned}
d &\approx r - \frac{r^2\mu^2 t^2}{2c(\tau - \tau_*) - r\mu^2 t^2} &\quad \text{local to pulsar,} \\
d &\approx \frac{2cr(\tau - \tau_*)}{2c(\tau - \tau_*) + r\mu^2 t^2} &\quad \text{half} - \text{way,} \\
d &\approx \sqrt{\frac{r^2}{4} + \frac{2cr(\tau - \tau_*)}{\mu^2 t^2}} - \frac{r}{2} &\quad \text{local to Earth.}
\end{aligned}
\tag{A7}
$$

Finally, from geometrical considerations and the assumptions made above, the deflection angle δ is given by

$$
\begin{aligned}
\delta &\approx \frac{\pi - \theta}{2} = \frac{\pi}{2} - \frac{\mu t}{2}\sqrt{\frac{\tau}{\tau - \tau_*}} &\quad \text{local to pulsar,} \\
\delta &\approx 2\theta = 2\mu t\sqrt{\frac{\tau}{\tau - \tau_*}} &\quad \text{half} - \text{way,} \\
\delta &\approx \pi - \theta = \pi - \mu t\sqrt{\frac{\tau}{\tau - \tau_*}} &\quad \text{local to Earth.}
\end{aligned}
\tag{A8}
$$

We applied equations (A7) to the echoes reported by Lyne et al. (2001) in the Crab pulsar in order to have a comparison between different models. Considering a delay of 7 ms 50 d before the closest approach, Lyne et al. (2001) find a distance of 1.3 pc between the pulsar and the IISM structure. Graham Smith, Lyne & Jordan (2011) find a distance of 5 pc for the same event, although they argue that this result could be overestimated. Using their same parameters, we find $x \sim 2.5$ pc using a pulsar distance of 1.7 kpc derived by Cordes & Lazio (2002). However, this result does not consider the motion of the lens with respect to the pulsar's LoS. Given also the large uncertainty expected from the limited knowledge of the pulsar distance and proper motion, we consider the three values to be reasonably consistent.

This paper has been typeset from a T_EX/L^AT_EX file prepared by the author.